Amphibian sacculus and the forced Kuramoto model with intrinsic noise and frequency dispersion

Seung Ji, Dolores Bozovic, and Robijn Bruinsma

Phys. Rev. E **97**, 042411 — Published 13 April 2018

DOI: 10.1103/PhysRevE.97.042411

The Amphibian Sacculus and the forced Kuramoto model with intrinsic noise and frequency dispersion

Seung Ji
Department of Physical Science, Los Angeles Mission College, Sylmar,CA

Dolores Bozovic
Department of Physics & Astronomy, University of California, Los Angeles,CA and California Nanosystem Institute, University of California, Los Angeles,CA

Robijn Bruinsma
Department of Physics University of California, Los Angeles, CA and Department of Chemistry and Biochemistry, University of California, Los Angeles, CA

The amphibian sacculus (AS) is an end organ that specializes in the detection of low-frequency auditory and vestibular signals. In this paper, we propose a model for the AS in the form of an array of phase oscillators with long-range coupling, subject to a steady load that suppresses spontaneous oscillations. The array is exposed to significant levels of frequency dispersion and intrinsic noise. We show that such an array can be a sensitive and robust sub-treshold detector of low-frequency stimuli, though without significant frequency selectivity. The effects of intrinsic noise and frequency dispersion are contrasted. Intermediate levels of intrinsic noise greatly enhance the sensitivity through *stochastic resonance*. Frequency dispersion, on the other hand, only degrades detection sensitivity. However, frequency dispersion can play a useful role in terms of the suppression of spontaneous activity. As a model for the AS, the array parameters are such that the system is poised near a saddle-node bifurcation on an invariant circle bifurcation. However, by a change of array parameters, the same system also can be poised near an *emergent* Andronov-Hopf bifurcation and thereby function as a frequency-selective detector.

I. INTRODUCTION

The sense of hearing constitutes a remarkable example of a biological system that operates near the physical limits of detection [1, 2]. Hair cells of the inner ear detect air-borne or ground-borne vibrations through the induced deflection of stereociliary bundles on their apical surface. Displacement of these *hair bundles* away from their resting positions are transduced into electrical signals by mechanically sensitive ion channels [3]. Thermal noise induces fluctuations in the bundle position on the order of a few nanometers; the hair cells nevertheless display sensitivity to signals of smaller amplitude, reaching into the sub-thermal range [4]. Moreover, the sensory epithelium is immersed in a dissipative fluid environment, ruling out passive mechanical resonance as an explanation for the frequency selectivity of hearing [5]. In 1948, Thomas Gold proposed that the auditory system must contain an internal energy-consuming amplifier that allows it to sustain its sensitivity of detection under overdamped conditions [6].

The phenomenology of *active* hearing has been analyzed using the mathematics of *bifurcation theory* [7–10]. Specifically, the sensitivity and frequency selectivity of the mammalian cochlea has been described as a dynamical system operating at or near the critical point of an *Andronov-Hopf bifurcation*. Crossing of this bifurcation is characterized by the amplitude of a stable limit cycle decreasing continuously to zero, at a constant frequency [11]. The Normal Form Equation (NFE) of the Andronov-Hopf bifurcation was found to reproduce a number of *in vivo* phenomena [7, 10], as well as measurements performed *in vitro* on individual hair bundles, including compressive nonlinearity and two-tone interference [12, 13].

A second bifurcation type that has been applied to describe hair cell dynamics is the *SNIC bifurcation* ("saddle-node on an invariant circle"). This bifurcation is characterized by a limit cycle of fixed amplitude whose frequency vanishes at the critical point. In this case, the normal form equation takes the form of the *Adler equation* for phase oscillators [11]. The SNIC bifurcation was introduced to describe the *in vitro* response of individual hair cell bundles of the amphibian sacculus (AS), exposed to a weak mechanical stimulus [14].

The AS – the focus of this paper – is an end organ that specializes in the detection of low-frequency (20-120Hz) auditory and vestibular signals. It is sensitive to extremely weak stimuli, but in contrast to the mammalian cochlea, it displays only broad frequency selectivity [15]. The AS has been an important model system for *in vitro* studies of hair bundle dynamics, because its robustness allows extensive mechanical measurements. Individual, unconstrained hair bundles of AS cells exhibit noisy spontaneous oscillations with amplitudes in the 50 nm range [16]. Nevertheless, periodic stimuli of much smaller amplitude are capable of *mode-locking* the noisy active motility [12, 17]. Under these conditions, AS hair cells are not poised in the vicinity of an Andronov-Hopf bifurcation, but rather in the limit cycle regime. The phase entrainment of hair cells adopts the form of an *Arnold tongue*, the region of synchronization to a periodic stimulus of varying stimulus amplitude and frequency [18].

Stimulus detection by the AS may be based on phase entrainment of innately active oscillators. However, spontaneous oscillations have only been observed *in vitro* in preparations that include a significant perturbation of the natural conditions: the overlying *otolithic membrane* – a gelatinous layer attached to the tips of the stereocilia – is removed to allow access to individual cells. Under *in vivo* conditions of the AS, the otolithic membrane imposes coupling between the bundles [19]. Removal of the membrane therefore decouples the cells, and also changes their natural mechanical loading. In semi-intact preparations that maintained the natural loading of the AS, hair bundles were imaged through an intact overlying membrane, and found to be *quiescent*. Upon removal of the membrane, the same hair bundles displayed robust spontaneous activity [20, 21]. These findings indicate that the *in vivo* signal detection mechanism of the AS is more likely to operate from the quiescent state. In an earlier study, we modeled a hair cell with the noisy Adler equation, with the control parameter poising it in the quiescent regime, and showed that it could act as a sensitive *sub-threshold detector*. Weak external signals were found to increase the probability that the system is activated above the threshold to perform one or more limit cycles [22].

Another important property of the AS that is not captured by studies of isolated hair cells is that of *frequency dispersion*. Experimental studies have shown that there is a broad distribution of natural frequencies of spontaneous oscillation, spread uniformly across the epithelium [23]. Neighboring hair bundles thus may exhibit quite disparate natural frequencies. This frequency dispersion seems consistent with the empirical observation that the frequency selectivity of the AS *in vivo* is very broad. One would expect, however, that in the absence of coupling, the ability of an array of noisy Adler oscillators to perform subthreshold detection would be degraded by frequency dispersion (see Section II). This consideration indicates that coupling likely plays an important role in achieving the sensitive signal detection displayed by the AS.

Several studies have addressed the effects of coupling on the response characteristics of hair cells. An experimental study that imposed coupling on a single oscillating hair bundle to its "cyber clone" encountered synchronization between the two [24]. A theoretical study of an array of hair cells reported that coupling leads to an enhanced sensitivity and frequency selectivity of the system [25]. Another study showed that while the critical point of an individual Hopf oscillator is concealed by intrinsic noise, a large array of coupled Hopf oscillators exhibits a well-defined phase transition separating the quiescent and active states [26]. Numerical simulations also demonstrated that systems of coupled hair cells with a large frequency disparity can exhibit *amplitude death* [27]. This is a phenomenon in which the limit cycles exhibited by two or more nonlinear oscillators with different frequencies are "quenched" by coupling. The quiescence of the AS was proposed to be a manifestation of amplitude death, leading to a state that could improve the signal-to-noise ratio (SNR) of detection by suppression of the noisy innate activity.

The aim of this paper is to study the response of a coupled array of sub-threshold phase oscillators subject to intrinsic noise and exhibiting frequency dispersion, to evaluate it as a possible model for stimulus detection by the AS.

The model is defined in Section II. In the absence of a stimulus or intrinsic noise, this model reduces to the *forced Kuramoto model* with frequency dispersion [28]. The latter is, in turn, an extension of the well-known Kuramoto model for phase synchronization of coupled oscillators, which includes a steady load that can suppress the spontaneous oscillations. The Arnold Tongue diagram of the forced Kuramoto model has been established analytically [28] in the absence of intrinsic noise. In the thermodynamic limit, where the number of coupled oscillators goes to infinity, this coupled-oscillator array can collectively exhibit the SNIC and Andronov-Hopf bifurcations, similar to those observed in single nonlinear oscillators. Note that in this case, the Andronov-Hopf bifurcation is an emergent property of the array, while individual phase oscillators do not exhibit the Andronov-Hopf bifurcation.

In Section III, we apply Dynamical Mean Field Theory (DMFT) to establish the bifurcation diagram of the forced Kuramoto model with both intrinsic noise and frequency dispersion and compare the results with numerical simulations of a finite array of 400 oscillators. We show that within the DMFT, the intrinsic noise and frequency dispersion exert similar effects.

In Section IV, we focus on the response of the model to a periodic stimulus. Over the range of parameters where the SNIC dominates, the array functions as a broadband low-frequency "seismic" detector with a large SNR. We find that the effects of intrinsic noise and frequency dispersion on the dynamical response are highly asymmetric. Intermediate levels of intrinsic noise can strongly *enhance* detection sensitivity through the *Stochastic Resonance* mechanism (SR) [29]. On the other hand, the model does not exhibit SR-type effects upon the introduction of frequency dispersion. However, we do observe that increasing levels of frequency dispersion can suppress the autonomous activity and thereby enhance detection sensitivity, consistent with the proposed amplitude death [27].

In short, the model array acts as a sensitive but robust subthreshold signal detector over intermediate levels of noise intensity and over intermediate levels of coupling, thus providing a viable model for the AS. For higher natural frequencies and for higher forcing amplitudes, the array exhibits an Andronov-Hopf bifurcation, rather than the SNIC. Near this bifurcation, the array can function as a sensitive *frequency-selective* detector. Though this is not a viable model for the AS, the ability of the array to shift from SNIC to an Andronov-Hopf bifurcation by a simple change of parameter values suggests that similar models may also capture the dynamics of auditory end organs.

II. ARRAY OF STOCHASTIC ADLER OSCILLATORS

We begin in this section by defining the equation of motion of a single phase oscillator and then extend it to a coupled array. Next, we introduce the Kuramoto order parameter and use it to interpret the results of numerical simulations for the response of the array.

A. Driven Stochastic Adler Equation

A number of models, of varying complexity, have been proposed to describe the motion of a hair bundle (see for example [30], [31]). One simple theoretical model of the auditory response is based on the Andronov-Hopf bifurcation [7]. In this model, the spontaneously oscillating system exhibits an amplitude that is determined by an internal control parameter. In this paper, we focus on the regime of oscillation far from the bifurcation, in which the amplitude can be treated as a constant, and the individual oscillator can be described by an equation for the time evolution of the phase. This simplification of the normal form equation yields a driven version of the well-known stochastic Adler equation (see Appendix A). The equation of motion for the phase degree of freedom θ, in dimensionless units, is given by:

$$\frac{\mathrm{d}\theta}{\mathrm{d}\tau} = \omega_0 - f_0 \sin\theta + f_\Omega \sin(\theta - \Omega\tau) + \xi(\tau) \qquad (1)$$

The dimensionless time τ denotes the actual time multiplied by the mean angular frequency of the hair bundles of the AS (about 190 rad/sec). The dimensionless natural frequency ω_0 is the natural angular frequency of a particular hair bundle, divided by the mean angular frequency (the mean value of ω_0 thus equals one). Next, f_0 is a steady force exerted on the hair bundle ("load') – which may be ramped in time – divided by the typical hydrodynamic drag force exerted on an unconstrained, spontaneously oscillating hair bundle (about 25 pN). Likewise, f_Ω is a force exerted by a periodic external drive divided by the typical drag force. The angular frequency of the drive equals Ω times the mean angular frequency. In micromechanical experiments performed *in vitro*, both f_0 and f_Ω are typically imposed by a piezoelectrically-driven fiber attached to the hair bundle. Under *in vivo* conditions, f_0 is the force exerted by the otolithic membrane [19], while f_Ω is the force exerted by an acoustic or seismic stimulus. Finally, $\xi(\tau)$ is a dimensionless variable that represents the noise to which a hair bundle is exposed. It is assumed, for mathematical convenience, to be a Gaussian random variable with autocorrelation function $\langle\xi(\tau)\xi(0)\rangle = 2D_\theta\delta(\tau)$, where D_θ has the physical meaning of the *phase diffusion coefficient*. In an earlier study [17], we showed that a number of measured characteristics of single hair bundle dynamics, such as phase diffusion, phase entrainment, and phase slips, are reproduced satisfactorily by this equation, with D_θ of the order of one.

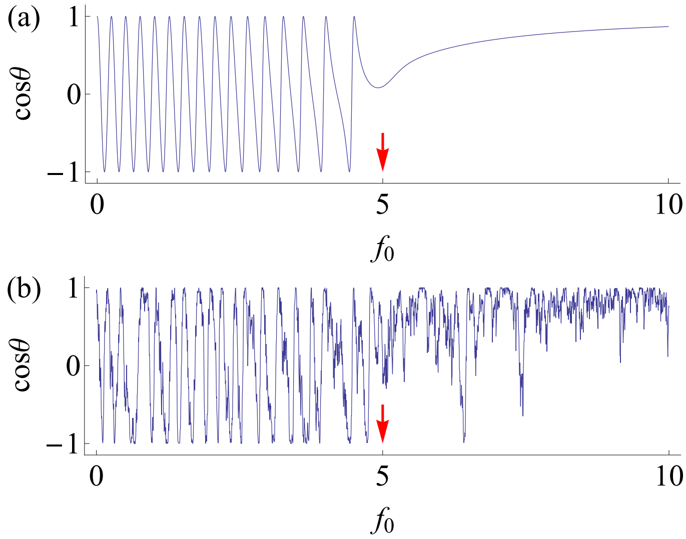

FIG. 1. Solutions of Eq.1, with $\omega_0 = 5$ and with a load $f_0(\tau) = 0.044\,\tau$ that is slowly ramped in time, obtained without noise (a, $D_\theta = 0$) and with noise (b, $D_\theta = 1$). The red arrow indicates the saddle-node bifurcation threshold $f_0 = \omega_0 = 5$.

The Adler equation itself (i.e., Eq. 1 with $D_\theta = f_\Omega = 0$) is familiar from the physics of Josephson Junctions and the driven pendulum [11]. It describes the transition from a quiescent to a dynamical state, characterized by a periodic train of spikes (i.e., phase slips of 2π, occurring from the quiescent state). The spike frequency goes continuously to zero at the threshold $f_0 = |\omega_0|$. In dynamical systems theory, the Adler equation is the standard equation that illustrates the saddle-node bifurcation [11]. If the oscillator is exposed to a periodic stimulus, so if $f_\Omega \neq 0$, then for $D_\theta = f_0 = 0$, the bifurcation occurs at $f_\Omega = |\omega_0|$, in the form of a transition between a state in which the phase precesses with frequency Ω ($\theta(\tau) = \Omega\tau + constant$) to a state in which a train of periodic phase-slips is superimposed on the phase precession.

Figure 1 compares examples of numerical solutions of Eq.1 for the noise-free case (a, $D_\theta = 0$) and for the case with noise (b, $D_\theta = 1$). The load $f_0(\tau) = 0.044\,\tau$ is slowly ramped in time, while $f_\Omega = 0$ in both cases. The red arrow indicates the bifurcation threshold $f_0 = \omega_0 = 5$. In the above-threshold regime, the system undergoes nonlinear oscillations whose frequency is reduced to zero at the threshold $f_0 = 5$ (red arrow). Below threshold the system is quasi-static. In the presence of noise, there is no clear bifurcation threshold. Importantly, stochastic spike events persist below threshold.

B. Array of Decoupled Oscillators

We previously showed that, in the absence of coupling, an ensemble of noisy, sub-threshold Adler oscillators can function as a remarkably sensitive broadband detector [22]. A stimulus that is too weak to activate the oscillator in the absence of noise still can modulate the statistical probability for a noise-triggered spike. This is illustrated in Fig. 2(a), which shows the result of superimposing 400 separate realizations of the numerical solutions of the subthreshold, driven, noisy Adler equation, in the presence of a weak stimulus (with a frequency $\Omega = \omega_0/4$). Though *individual* oscillators only rarely undergo a phase-slip event, when it occurs, it does so at a preferred phase of the stimulus. It follows that for a sufficiently large array, there is always a subset of oscillators that spikes at the preferred phase of each stimulus cycle. The spiking of a large array of decoupled noisy Adler oscillators, exhibiting the same natural frequency, is thus synchronized with respect to the stimulus. The presence of intrinsic noise is essential here, as there would be no phase-slip events in the absence of fluctuations. When the noise amplitude, determined by D_θ, was varied, the signal-to-noise ratio (SNR) exhibited a maximum at intermediate values of D_θ, an example of the stochastic resonance phenomenon.

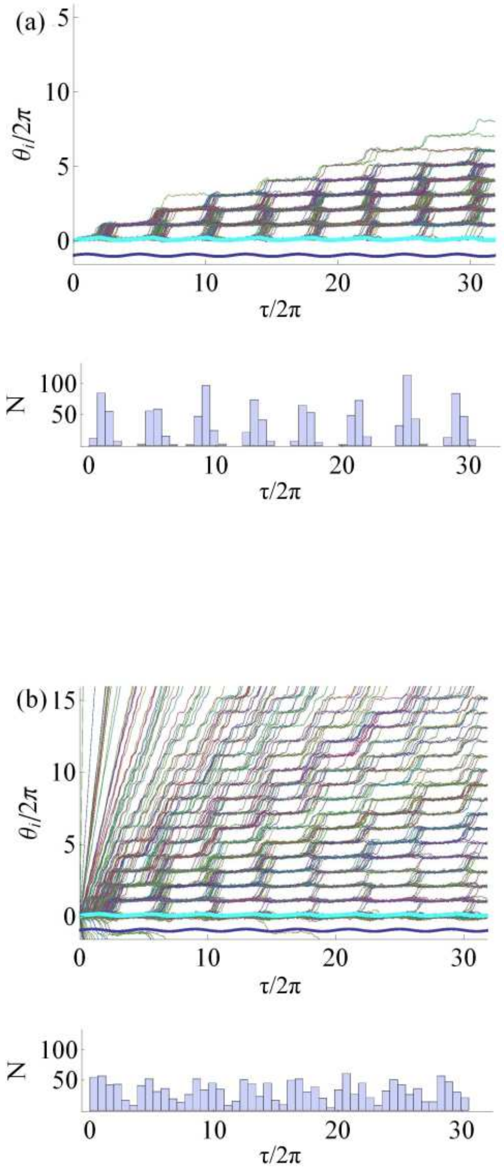

FIG. 2. Superposition of 400 sub-threshold, uncoupled hair bundles that obey Eq.1 with $D_\theta = 0.05$, $\omega_0 = 1$, $f_0 = 1.15$, $\Omega = 0.25$, and $f_\Omega = 0.1$. The bottom panels show the number of oscillators N that undergo a phase slip event in a fixed time window. Blue line: stimulus. (a) No frequency dispersion is introduced ($\Delta = 0$). (b) The oscillators exhibit frequency dispersion ($\Delta = 0.5$).

In order to examine the effects of introducing a frequency dispersion among the hair bundles, we assumed a Lorentzian probability distribution $g(\omega_0)$ for the natural frequencies, with a mean equal to one:

$$g(\omega_0) = \frac{\Delta}{\pi}\frac{1}{(\omega_0 - 1)^2 + \Delta^2} \tag{2}$$

The (dimensionless) width Δ is a measure of the frequency dispersion. For the case of the AS, Δ is estimated to be of the order of 0.5. The top panel of Fig. 2(b) shows the superimposed time traces of the oscillator phases for $\Delta = 0.5$. In this case, there is in general a fraction of oscillators with natural frequencies above threshold. This corresponds to the phase trajectories that steeply increase in time. The bottom panel, showing the spike histogram, indicates that the detection sensitivity has been significantly degraded in comparison with the dispersion-free case in Figure 2(a). In the presence of strong frequency dispersion, an array of decoupled noisy Adler oscillators could not be a sensitive detector of weak stimuli. In the subsequent sections, we will explore the effects of coupling the hair bundles.

C. Driven Noisy Kuramoto-Adler Model (DNKA)

The equations of motion for a coupled array of noisy driven Adler phase oscillators are:

$$\begin{aligned}\frac{\mathrm{d}\theta_i}{\mathrm{d}\tau} =& \,\omega_{0i} - f_0 \sin\theta_i + f_\Omega \sin(\theta_i - \Omega\tau) + \xi_i(\tau) \\ & - \frac{1}{N}\sum_{j=1}^{N} K_{i,j}\sin(\theta_i - \theta_j)\end{aligned} \tag{3}$$

which we will refer to as the Driven Noisy Kuramoto-Adler Model (DNKA) model. Here, $\theta_{i=1..N}$ are the phase degrees of freedom of N hair bundles, while the $K_{i,j}/N$ are dimensionless coupling constants between hair bundles i and j such that $K_{i,j}/N$ is the force exerted by hair bundle i on hair bundle j in units of the typical drag force. The physical origin of the coupling is as follows. As already mentioned, hair cells of the sacculus are coupled by an overlying otolithic membrane [19]. The simplest continuum theory model for the membrane treats it as a uniform, two dimensional elastic sheet. In Appendix A, we show that in that case, the coupling constant $K_{i,j}$

decays very slowly with the separation $|r_{i,j}|$ between the oscillators, following $1/\log(r_{i,j}/a)$ dependence, where a denotes the mean spacing between the hair bundles of the AS. When applied to the AS, $r_{i,j}/a$ does not exceed 10^3 so as a reasonable approximation, we replace the coefficients $K_{i,j}$ with a single constant K (estimated to be of the order of 10 for the AS [32]). Finally, the same load f_0 and sinusoidal stimulus f_Ω is exerted on each oscillator of the system.

D. Order parameter

In the thermodynamic limit $N \to \infty$, many-body systems with infinite-range coupling, such as the DNKA model with $K_{i,j} = K$, can be treated exactly by *mean-field* theory. The response of a system in this limit can be characterized in terms of an order parameter. For the DNKA model, this is the Kuramoto order parameter:

$$r(\tau)e^{i\psi(\tau)} = \frac{1}{N}\sum_j e^{i\theta_j(\tau)}. \qquad (4)$$

In the absence of applied forces or stimuli (i.e., $f_0 = f_\Omega = 0$), the dynamical mean-field theory (DMFT) for the Kuramoto order parameter can be shown to describe a separate bifurcation transition, at a critical coupling constant K_c, from an incoherent state with $r = 0$ to a coherent state with non-zero r. For the Lorentzian frequency distribution, the critical coupling constant is $K_c = 2(D_\theta + \Delta)$. The transition has the character of a second-order phase transition with the order parameter going to zero continuously as $\rho = \sqrt{1 - K_c/K}$ [33, 34]. Note, from the expression for K_c, that intrinsic noise and frequency dispersion appear to combine in an additive manner. It would seem that frequency dispersion simply provides a second source of noise, with an effective phase diffusion coefficient Δ.

Figure 3 shows the superimposed trajectories of a system of 400 phase-oscillators with a coupling constant $K = 15$ for increasing noise levels D_θ. The remaining parameters are the same as in Fig. 2(b) with a frequency dispersion $\Delta = 0.5$, load $f_0 = 1.15$, stimulus amplitude $f_\Omega = 0.1$, and stimulus frequency $\Omega = 0.25$. The system is thus *on average* below threshold. The phase ψ of the order parameter is shown in Figure 3 as a light blue line (thick light gray line in print). For $D_\theta = 0.5$, the noise level is already sufficiently high to allow for the occurrence of sporadic, incoherent phase-slip events. For $D_\theta = 2.5$, a sequence of collective phase-slip events is triggered at a specific phase of the stimulus. The order parameter now rotates in the complex plane in phase with the periodic stimulus. Up to this point, K was larger than the critical value $K_c = 2(D_\theta + \Delta)$ for phase synchronization. If the noise level is increased to $D_\theta = 8$, which means that K is less than K_c, then the noise triggers an avalanche of phase slips. Phase coherence with the stimulus is lost. The time-averaged amplitude r_{ave} of the order parameter steadily decreases to zero as the noise level increases (Figure 3(d)).

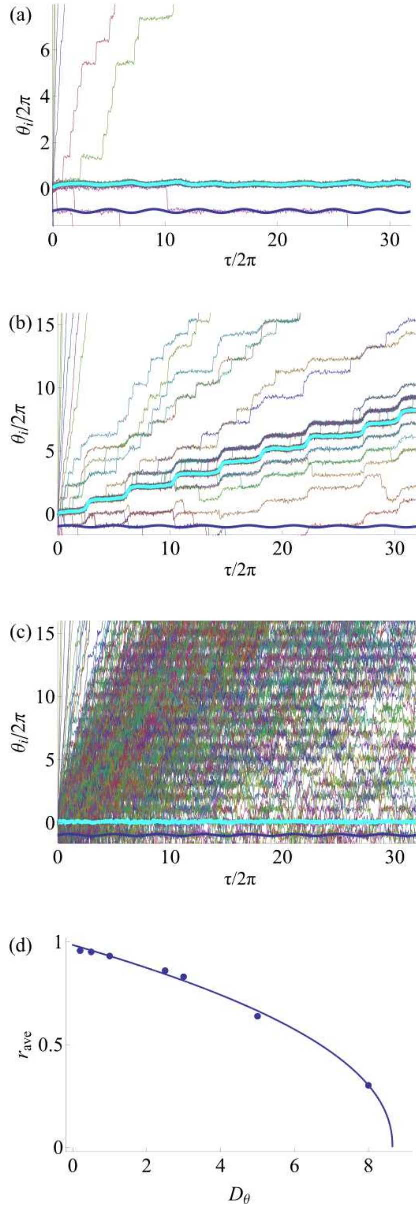

FIG. 3. Superposition of 400 coupled hair bundles that obey Eq.3 with $\Delta = 0.5$, $f_0 = 1.15$, $\Omega = 0.25$, $f_\Omega = 0.1$, and $K = 15$. The noise intensity increases: (a) $D_\theta = 0.5$, (b)$D_\theta = 2.5$, and (c) $D_\theta = 8$. Light blue (thick light gray) lines show the phase of the order parameter. Blue (black) lines indicate the sinusoidal stimulus. The time-averaged order parameter amplitude r_{ave} is shown separately in (d). The solid line indicates a numerical fit of the data.

III. DYNAMICAL MEAN-FIELD THEORY

In this section, we discuss the dynamical mean field theory (DMFT) phase diagram of the DNKA model for non-zero steady load f_0 with both intrinsic noise and frequency dispersion. No stimulus is introduced in this section. We define $\rho_{\omega_0,\tau}(\theta)$ to be the probability distribution of the phase degrees of oscillators with natural frequency ω_0. The full probability distribution is $\rho_{\omega_0,\tau}(\theta)g(\omega_0)$, where $g(\omega_0)$ is the Lorentzian frequency distribution. The time-dependent order parameter is ob-

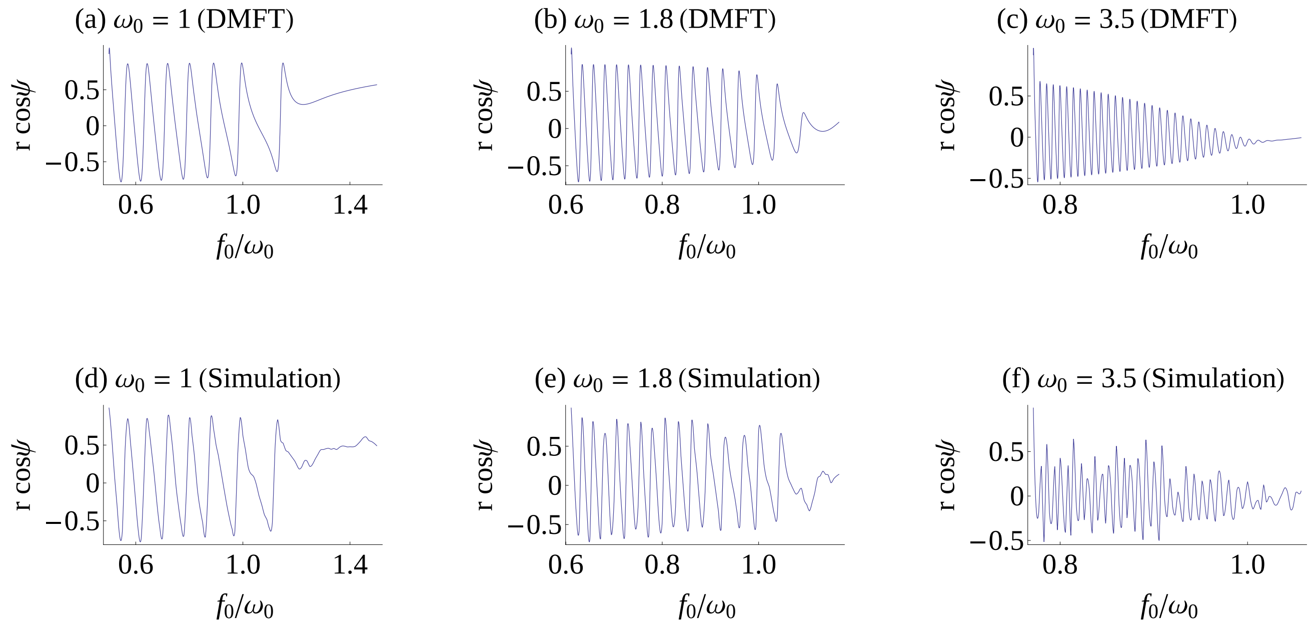

FIG. 4. Solutions of the DMFT equations in the absence of frequency dispersion by the spectral method (top row), as compared with numerical solution of the equations of motion for 400 coupled noisy Adler phase-oscillators (bottom row). System parameters: $K = 4$, $D_\theta = 1$, and $f_\Omega = 0$. The load $f_0(\tau)$ slowly increases in time ($\mathrm{d}f_0/\mathrm{d}\tau = 1/100$). The natural frequency is (a) $\omega_0 = 1$, (b) $\omega_0 = 1.8$, and (c) $\omega_0 = 3.5$. Depending on the value of the parameter, the system undergoes different types of bifurcation: (a) and (d) show a SNIC bifurcation, (c) and (f) show an Andronov-Hopf bifurcation, and (b) and (e) show a Bogdanov-Takens bifurcation. The three bifurcation points described here are also indicated in Figure 6.

tained from the distribution $\rho_{\omega_0}(\theta,\tau)g(\omega_0)$ through

$$re^{i\psi} = \int_0^{2\pi}\int_{-\infty}^{\infty} e^{i\theta}\rho_{\omega_0}(\theta,\tau)g(\omega_0)\,\mathrm{d}\theta\,\mathrm{d}\omega_0 \tag{5}$$

The probability distribution $\rho_{\omega_0}(\theta,\tau)$ is the solution of the Fokker-Planck (FP) equation for the DNKA model given by:

$$\frac{\partial\rho}{\partial\tau} = D_\theta\frac{\partial^2\rho}{\partial\theta^2} - \frac{\partial}{\partial\theta}[(\omega_0 - f_0\sin\theta + Kr(\tau)\sin(\psi(\tau)-\theta))\rho] \tag{6}$$

Equations 5 and 6 are a pair of self-consistent equations that define the DMFT: the FP equation depends on the time-dependent order parameter, while the order parameter is determined by the solution of the FP equation. Taking the time derivative of Eq.4, and using the FP equation, we obtain the following equations for the order parameter:

$$\frac{\mathrm{d}r}{\mathrm{d}\tau} = -(D_\theta+\Delta)r + (1-\sigma_r^2)(Kr + f_0\cos\psi) + \beta^2 f_0\sin\psi \tag{7a}$$

$$\frac{\mathrm{d}\psi}{\mathrm{d}\tau} = \omega_0 - f_0(\sigma_r^2/r)\sin\psi - \beta^2(K + (f_0/r))\cos\psi \tag{7b}$$

Here, $\sigma_r^2 = \langle\cos^2(\theta-\psi)\rangle$ is a measure of the fluctuations of the phase angle of individual oscillators with respect to that of the order parameter, while $\beta^2 = \langle\cos(\theta-\psi)\sin(\theta-\psi)\rangle$ is a measure of the *asymmetry* of the angle distribution function around the mean. Note that the combination $(D_\theta+\Delta)$ appearing in the first equation again suggests that intrinsic noise and frequency dispersion contribute in a similar fashion, in this case to the decay rate of the order parameter amplitude. The averages $< ... >$ must be computed with respect to the full probability distribution $\rho_{\omega_0}(\theta,\tau)g(\omega_0)$. In the next sections, we will discuss solutions for the pair of coupled equations by two different methods.

A. Spectral Method

The "spectral method" [34] focuses on the time-dependent complex Fourier amplitudes of the probability distribution:

$$z_n(\tau) = \int_0^{2\pi}\mathrm{d}\theta\int_{-\infty}^{\infty}\mathrm{d}\omega_0\, e^{in\theta}\rho_{\omega_0}(\theta,\tau)g(\omega_0) \tag{8}$$

Note that $z_0 = 1$, while z_1 is the order parameter with z_{-1} its complex conjugate. Taking the derivative with respect to time, and using the FP equation, we obtain a hierarchy of coupled first-order differential equations

$$\begin{aligned}\frac{\mathrm{d}z_n}{\mathrm{d}\tau} &= (in\omega_0 - n^2D_\theta - n\Delta)z_n + \\ &+ \frac{n}{2}(Kz_1+f_0)z_{n-1} - \frac{n}{2}(Kz_{-1}+f_0)z_{n+1}\end{aligned} \tag{9}$$

The hierarchy can be truncated for larger n, since the decay rate of the high-frequency modes increases as n^2, due to the intrinsic noise. Note that intrinsic noise and frequency dispersion here act in a different manner: the contribution due to the frequency dispersion grows only linearly with n. This set of equations is soluble for $D_\theta = 0$ [28], but for non-zero D_θ, one must seek numerical solutions. To that purpose, we treat the array $\vec{Z}(\tau) \equiv (z_1, z_{-1}, z_2, z_{-2}.......z_M, z_{-M})$ as a time-dependent vector in a $2M$-dimensional space, where we set the z_k with $|k| > M$ to be equal to zero. In the figures in this paper, $k = 80$; higher k values show same results. The trajectory of $\vec{Z}(\tau)$ can then be obtained by numerical integration, starting from a given initial state $\vec{Z}(\tau = 0)$, and continuing the integration until a steady state is reached that is independent of the initial conditions.

The solution of the DMFT is simplest in the absence of frequency dispersion ($\Delta = 0$), when the natural frequency ω_0 can be treated as a fixed parameter. Figure 4 compares the predictions of DMFT with a simulation of 400 coupled oscillators, for $K = 4$, $D_\theta = 1$, and different values of the natural frequency ω_0. The stimulus amplitude f_Ω was set to zero, while the load was slowly increased as a function of time, as in Figure 1. DMFT adequately reproduces the numerical results for $\omega_0 = 1$. The appearance of spontaneous oscillations has, in DMFT, the character of a saddle-node bifurcation, with the frequency going to zero at the bifurcation point. In fact, because the phase of the order parameter and the amplitude of the order parameter are separate dynamical variables, it is more accurate to call this a SNIC bifurcation.

For $\omega_0 = 1.8$, both the frequency and amplitude go to zero at the onset of spontaneous oscillations in DMFT. This is a characteristic of a Bogdanov-Takens (BT) bifurcation. When compared to numerical simulations, DMFT misses the higher harmonics. For $\omega_0 = 3.5$, the frequency remains constant, and the onset of spontaneous oscillations has the character of an Andronov-Hopf bifurcation. The "finite-N fluctuations" appear to have a stronger smearing effect on the Andronov-Hopf bifurcation than on the SNIC bifurctation.

B. Stationary States and Linear Stability

A second method of solving the DMFT starts from the FP equation with a time-independent order parameter:

$$D_\theta \frac{\partial^2 \rho}{\partial \theta^2} - \frac{\partial}{\partial \theta}[(\omega_0 - f_0 \sin\theta + Kr\sin(\psi - \theta))\rho] = 0 \quad (10)$$

This equation can be solved analytically [35], yielding explicit expressions for quantities σ_r^2 and β^2 in terms of r and ψ (see the Appendix B). The static order parameter is then obtained self-consistently from Eq. 7, with the left side set to zero. The stability limits are established by linearizing Eq. 7 around the static solutions. The nature of the bifurcation is determined from the linear stability analysis of these static solutions, which was

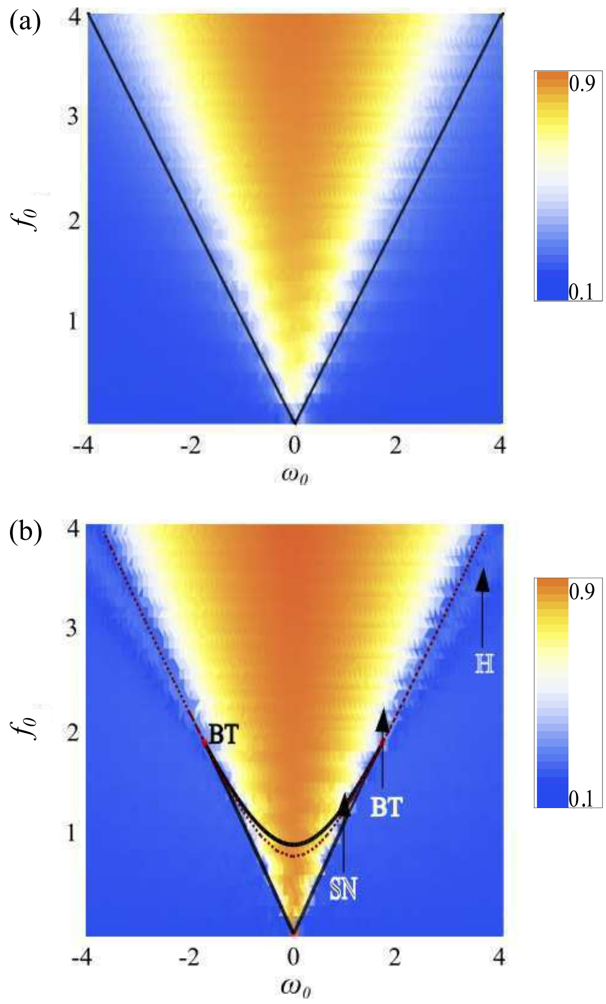

FIG. 5. Arnold Tongue: Order parameter obtained by the spectral method for $D_\theta = 1$ in the absence of frequency dispersion. (a) $K = 1.8$ and (b) $K = 4$. The horizontal axis is the natural frequency ω_0, and the vertical axis is the steady load f_0. The color scale represents the amplitude of the static order parameter. Red (bright): high amplitude; blue (dark): low amplitude. Inside the yellow-red colored (gray) wedge, the static order parameter is stable. The black line in the (a) represents the bifurcation line of a single Adler equation. For $K < K_c$, the order parameter undergoes an Andronov-Hopf bifurcation. The lines in (b) represent the different bifurcations obtained from the linear response theory with the stationary solution of the mean-field Fokker-Planck equation. H indicates an Andronov-Hopf bifurcation (red (dotted line)), SN a SNIC bifurcation (black), and BT a Bogdanov-Takens bifurcation. The three arrows correspond to the three time-traces in Figure 4.

performed using MatCont. The result is shown in Figure 5(b) and Figure 6. As before, we set the frequency dispersion to zero ($\Delta = 0$). The horizontal axis in Figure 5 is the average natural frequency ω_0, while the vertical axis is the steady load f_0. The color scale represents the amplitude of the zero-frequency component of the order parameter, with red (darker) shades representing higher amplitudes. For larger ω_0, the system enters the static state at progressively higher values of the imposed offset.

Solid lines represent the loci of bifurcations obtained from the linear stability analysis of Eq. 7. Black solid lines in Figure 5(a) denote SNIC bifurcations of a single Adler equation and mark the stability limits of the static solution. The delineated region of phase space is an example of an Arnold Tongue and the boundaries of the Arnold Tongue are aligned with the loci of bifurcations.

The bifurcation dynamics of the full system depends on the coupling strength. A single Adler equation undergoes a SNIC bifurcation. However, for $K < K_c$, the order parameter of the coupled array undergoes an Andronov-Hopf bifurcation, since the oscillators are in an incoherent state. In Figure 5(a)($K = 1.8 < K_c$), the Arnold Tongue shows a gradual increase of the order parameter, so the boundaries of the Arnold tongue are not aligned with the SNIC bifurcation lines (solid black lines). This indicates that the bifurcation is not a SNIC bifurcation when the coupling strength is below the critical coupling constant. For $K = 4$ (Figure 5(b)), the bifurcation diagram is more complex than in Figure 5(a). For small ω_0, the stability limit of the static solution remains a SNIC bifurcation, while for larger values of $|\omega_0|$, the stability limit of the static solution is an Andronov-Hopf bifurcation, shown as red dotted lines. Accordingly, for smaller ω_0, the *frequency* of the spontaneous oscillation goes to zero at the bifurcation, while for larger ω_0, it is the *amplitude* of the oscillation that goes to zero at the bifurcation. The crossover regime is more complex and includes a Bogdanov-Takens bifurcation, where both amplitude and frequency go to zero. Increasing the coupling between the phase oscillators thus not only enhances the phase coherence, it also alters the dynamics of mode-locking by introducing Hopf and BT bifurcations.

This mode-locking diagram is very similar to that obtained for a *single* oscillator using the Normal-Form Equation of the Andronov-Hopf bifurcation [36], which has two degrees of freedom. In the mean-field limit of large N, the many-oscillator model thus has a mode-locking bifurcation diagram that is similar to that of a dynamical system with only two coupled degrees of freedom.

We can combine the results of the spectral and linear-response methods. The three arrows in Figure 6, marked "SN", "BT", and "H", correspond to the three time traces obtained from the spectral method shown in Figure 4. The three time traces indeed correspond to the three amplitude-frequency signatures predicted by the linear response theory. In Figure 6, we show the average decay rate of the amplitude of the order parameter $\langle dr/d\tau\rangle$, as computed by the spectral method for $K = 4$, starting from $r = 1$. Dark blue (gray) region in Figure 6 denotes $\langle dr/d\tau\rangle = 0$, indicating that the order parameter is time independent, while the light blue (light gray) region, $\langle dr/d\tau\rangle \neq 0$, shows that the order parameter is oscillating. The color map of the order-parameter decay rate $\langle dr/d\tau\rangle$ displays the precise limits of the Arnold Tongue that are bounded by the bifurcation lines from the analysis of DMFT.

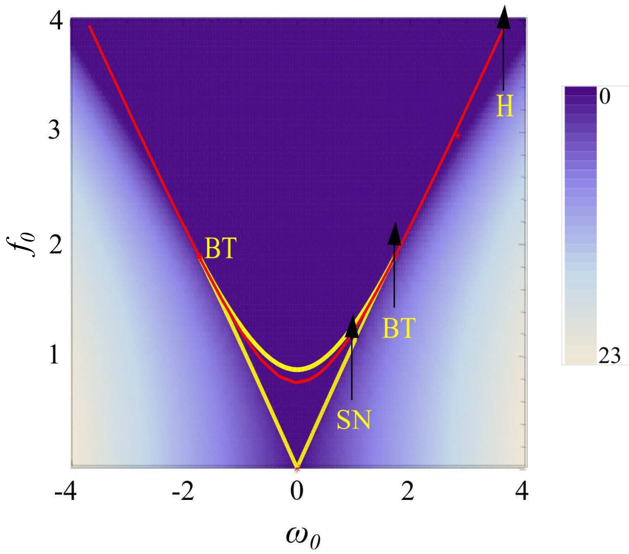

FIG. 6. Mode-locking diagram for $K = 4$ and $D_\theta = 1$ in the absence of frequency dispersion, as obtained by the spectral method. The horizontal axis is the mean natural frequency, and the vertical axis is the steady load. The color map represents time average of the time derivative ($\langle dr/d\tau\rangle$) of the order parameter amplitude r, starting from $r = 1$. Dark blue (dark gray) indicates that the order parameter does not decay with time, while lighter shades indicate increasing rates of decay of the order parameter. The lines indicate the bifurcations obtained by the linear-response theory, while the three arrows correspond to the three time traces of Figure 4.

C. Frequency Dispersion

With these preliminaries, we can now compare the effects of intrinsic noise and dispersion on coherent oscillations of the order parameter. One might expect that the bifurcation diagrams will be smeared out if ω_0 is a random variable. However, the sequence of SNIC, BT, and Andronov-Hopf bifurcations in DMFT we found for $\Delta = 0$ resembles that found for $D_\theta = 0$ but finite Δ in ref. [28].

We will compare the two cases by focusing on the *average decay rate of the order parameter*. We first do this for the case with negligible frequency dispersion. Figure 7 shows the average decay rate of the amplitude of the order parameter as a function of f_0 and D_θ (Figure 7(a)), and as a function of f_0 and Δ (Figure 7(b)). Dark blue (dark gray) indicates that the order parameter is independent of time, while lighter shades indicate a non-zero time derivative associated with order-parameter oscillations. The top figure shows the case of varying noise levels and negligible frequency dispersion. The horizontal axis is the noise level and the vertical axis the static offset f_0. For $f_0 = 0$ and varying D_θ, the order-parameter is time-dependent for D_θ less than ~ 2.0. This is the location of the Kuramoto synchronization transition for $K = 4$. For $D_\theta = 0$ and varying f_0, this transition occurs around $f_0 = 1$, which is the location of the SNIC bifurcation for $\omega_0 = 1$. As D_θ increases, the location of the onset of coherent oscillations does not change signif-

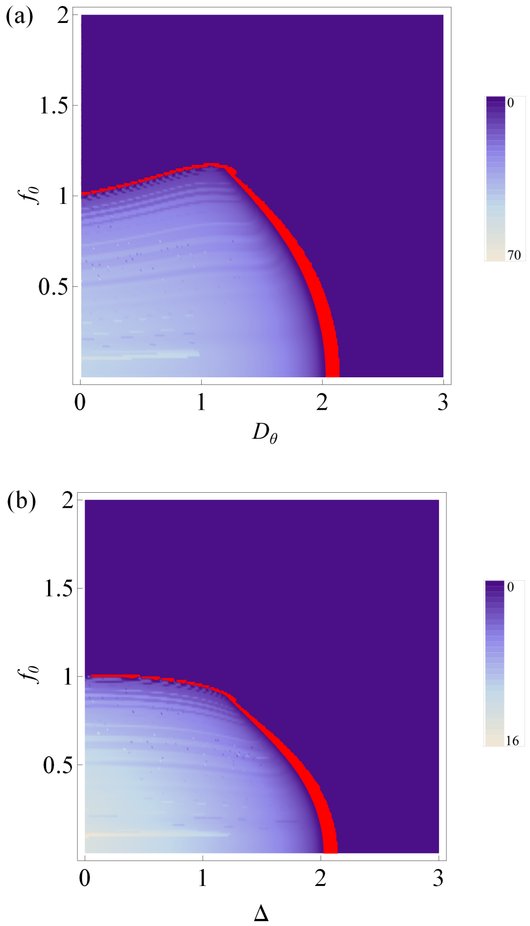

FIG. 7. Kuramoto Synchronization in the presence of noise (a) and frequency dispersion (b). The color map represents the time derivative of the order parameter amplitude. Dark blue (dark gray) indicates that the order parameter is time-independent, while lighter shades indicate that the order parameter is increasingly time dependent. Red (gray curves between two regions) lines indicate instability onset regions where $0 < \langle \mathrm{d}r/\mathrm{d}\tau \rangle < 0.08$. K=4 in both cases. (a) No frequency dispersion with $\omega_0 = 1$. Horizontal axis: noise level D_θ. Vertical axis: steady load f_0. (b) No noise. Horizontal axis: frequency dispersion Δ. Vertical axis: steady load f_0.

icantly, as long as D_θ is less than one. However, for D_θ greater than one, the threshold static offset for the occurrence of coherent oscillations rapidly decreases below $\omega_0 = 1$ with increasing D_θ, until it approaches the Kuramoto synchronization at $f_0 = 0$. The onset of coherent oscillations for f_0 less than $\omega_0 = 1$ has the character of an Andronov-Hopf bifurcation and can be viewed as a form of the Kuramoto synchronization threshold.

Next, Fig. 7(b) shows the case of varying frequency dispersion and negligible intrinsic phase noise. Two diagrams have some differences when $D_\theta < 1$ and $\Delta < 1$. The static offset for the bifurcation point slightly increases as D_θ increases, when $D_\theta < 1$. This implies that higher offset is required to reach the bifurcation point, because the system shows more robust coherent oscillations when an intermediate level of noise ($D_\theta < 1$) is introduced into the system. On the other hand, the offset point for the bifurcation decreases slightly as Δ decreases in Figure 7(b). This indicates that the spontaneous coherent oscillations degrade as the frequency dispersion increases. However, when $D_\theta > 1$ and $\Delta > 1$, the transition regions of the two figures are essentially similar and can be interpreted in the same manner. We conclude that, within DMFT and the spectral method, the effects of intrinsic noise and frequency dispersion are closely similar. Similar conclusions were drawn previously in refs. [33] and [37].

IV. STIMULUS DETECTION BY A COUPLED DNKA ARRAY

We now introduce the external stimulus into the coupled equations of motion in order to explore the detection sensitivity of the array. The equations of motion are now:

$$\begin{aligned}\frac{\mathrm{d}\theta_i}{\mathrm{d}\tau} &= \omega_i + Kr\sin(\theta_i - \psi) - f_0 \sin\theta_i \\ &- f_\Omega \sin(\theta_i - \Omega\tau) + \xi_i(\tau)\end{aligned} \tag{11}$$

The parameters f_0, K, Δ, and D_θ are chosen so that in the absence of stimulus ($f_\Omega = 0$), the system is poised in the quiescent region of the Arnold Tongue, but close to a bifurcation. The response of the array to an imposed stimulus is quantified by the power spectral density (PSD) of the order parameter $S(\omega)$, defined as:

$$S(\omega) = |\frac{1}{\sqrt{T}} \int_0^T r(\tau) e^{i\psi(\tau)} e^{-i\omega\tau} \, \mathrm{d}\tau|^2 \tag{12}$$

with T the measurement duration (in dimensionless units). The PSD has a peak at $\omega = 0$ with a width $1/T$. The signal-to-noise ratio (SNR) can be defined as

$$\mathrm{SNR} = \frac{S(\omega = \Omega)_{f_\Omega \neq 0}}{S(\omega = \Omega)_{f_\Omega = 0}} \tag{13}$$

A. Stimulus detection near the SNIC bifurcation

We first consider a system that is poised on the quiescent side of a SNIC bifurcation, and compute its response to a periodic stimulus. Figure 8 shows the results, obtained for the case with no dispersion ($\Delta = 0$). Panels (a)- (f) of the figure show the order parameter with stimulus, computed at different phase diffusion coefficients D_θ. After a brief transient, the order parameter amplitude r decreases with increasing D_θ. The order parameter phase is zero in all cases. For $D_\theta = 0.5$, the order parameter oscillates with a low amplitude at the drive frequency (Figure 8 (a)). Since $f_0 + f_\Omega = 1.25$ exceeds $\omega_0 = 1$, the system remains below threshold in the presence of the stimulus. The power spectrum has two small peaks, near $\Omega/2$ and Ω (Figure 8 (d)). If the noise

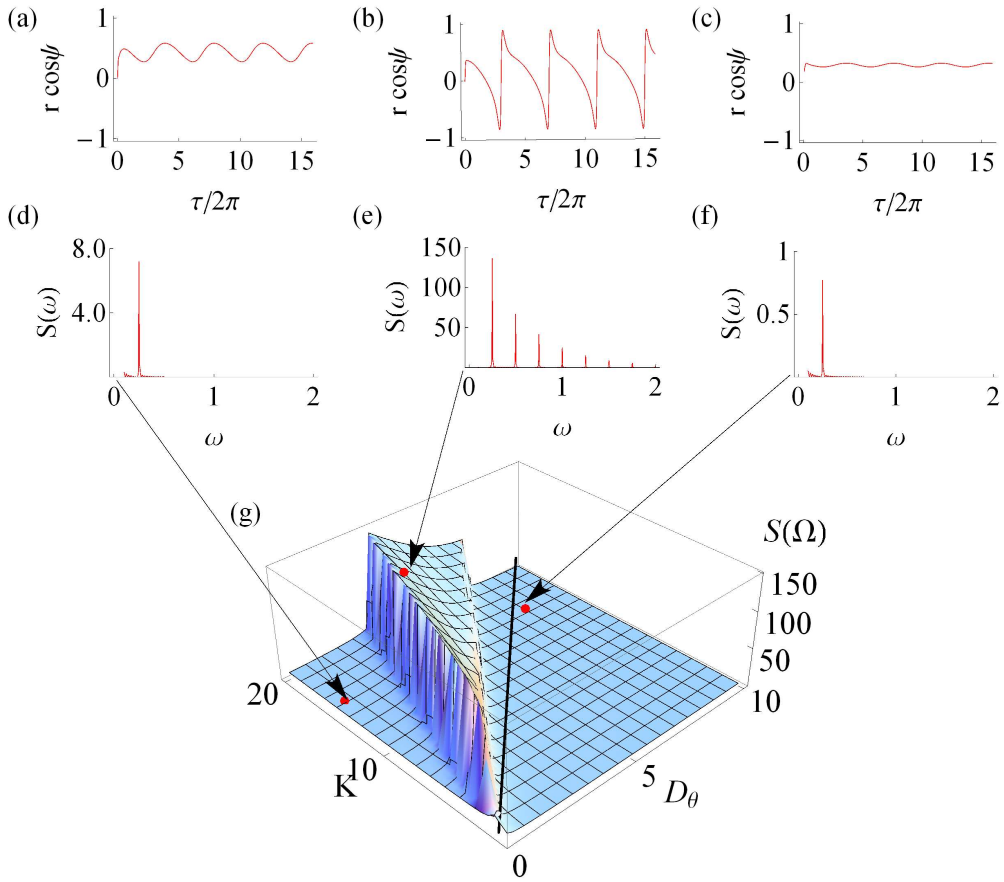

FIG. 8. Stochastic resonance near a SNIC bifurcation point in the absence of frequency dispersion. The response of a coupled DNKA array, poised near a saddle-node bifurcation, and subject to a sinusoidal stimulus. The system parameters are $K = 15$, $\omega_0 = 1.0$, and $f_0 = 1.15$. The stimulus frequency is $\Omega = 0.25$, and the stimulus amplitude is $f_\Omega = 0.1$. The top panels, (a)-(c), represent time-dependent real part of the order parameter, computed at three different values of the phase diffusion coefficient D_θ: (a) $D_\theta = 0.5$, (b) $D_\theta = 3$, and (c) $D_\theta = 8$. The bottom panels, (d)-(f), show the corresponding power spectra. (g) Power output $S(\omega = \Omega)$ as a function of the noise level D_θ and coupling constant K. Red (gray) dots in this panel represent K and D_θ values of plots shown in (a)-(f), as indicated by the arrows. The black line in (g) represents the Kuramoto transition line. The system exhibits clear stochastic resonance.

intensity is increased to $D_\theta = 3$, then the order parameter (Figure 8 (b)) exhibits a regular train of high amplitude limit-cycle spikes. The power spectrum (Figure 8 (e)) shows a harmonic series at integral multiples of the drive frequency Ω, which indicates $1:1$ mode-locking of the array to the drive. The response is, however, highly non-linear: the spike train bears little resemblance to the stimulus. The different amplitudes reflect the Fourier components of a single limit cycle at the harmonics of the fundamental frequency Ω. In this regime, the SNR is very large. Finally, when the noise level is raised to $D_\theta = 8$, the spike train collapses, and the response to the stimulus is negligibly small compared to $D_\theta = 3$.

The final panel, Figure 8 (g), shows the power output at the drive frequency, $S(\omega = \Omega)$, as a function of the noise level D_θ and coupling constant K. The power output shows a noise-induced enhancement, for intermediate levels of noise levels, a signature feature of stochastic resonance (SR). Increasing the coupling increases the range of D_θ values over which SR is effective and shifts it to higher values of D_θ. For fixed D_θ, the enhancement of the output power as a function of K is *also* restricted to a range of intermediate values of K. As K is increased, one encounters first a lower threshold value where the output power rapidly increases. The power output then continues to increase with K until an upper threshold is reached, where the power output precipitously drops to zero. The threshold for Kuramoto synchronization at $K_c = 2(D_\theta + \Delta)$ is indicated in Figure 8 with a solid black line. Hence, stimulus detection occurs only if the Kuramoto order parameter is well developed; however, if the coupling is too strong, the stimulus detection collapses.

Figure 9 shows a plot of the output power at the drive frequency ($S(\omega = \Omega)$), as a function of the drive amplitude f_Ω and the drive frequency Ω. Stimulus detection is restricted to lower frequencies. However, as the frequency is reduced, the output power diminishes, initially slowly, but then quite strongly at very low frequencies. However, the SNR remains large even when the frequency

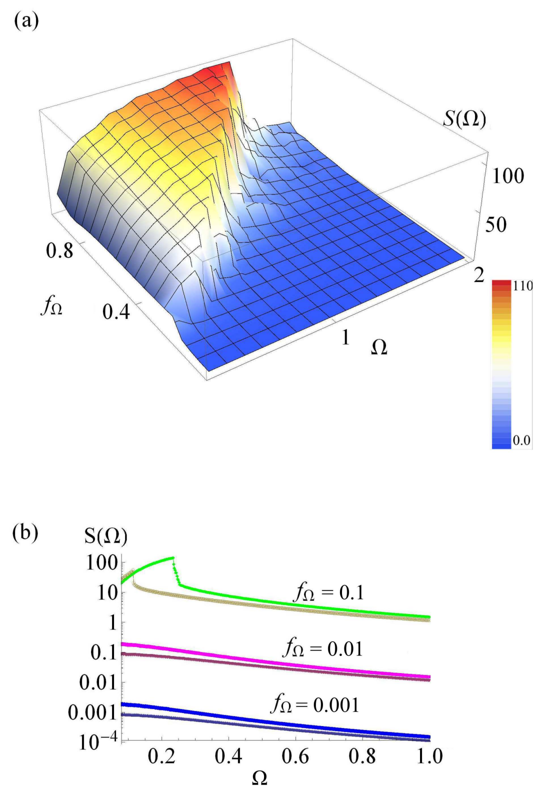

FIG. 9. Frequency selectivity near the SNIC bifurcation. (a) Power output $S(\omega = \Omega)$ as a function of the stimulus frequency Ω and stimulus amplitude f_Ω, for $D_\theta = 1$, $\Delta = 0$, $K = 15$, $f_0 = 1.15$. (b) Power output $S(\omega = \Omega)$ as a function of the stimulus frequency Ω, for various values of f_Ω $(0.001, 0.01, 0.1)$, and with $K = 15$, $D_\theta = 2.5$, and $f_0 = 1.15$. For $\Delta = 0$, the results are shown in bright green, bright magenta, and bright blue (light shades of gray, curves with slightly higher $S(\Omega)$ values for a given stimulus amplitude). For $\Delta = 1.5$, the curves are shown in dark green, dark magenta, and dark blue (dark shades of gray, curves with slightly lower $S(\Omega)$ values for a given stimulus amplitude). The coupled DNKA array clearly shows high SNR at low-frequency range. The frequency dispersion degrades the responsiveness, but the stochastic resonance is still present at low frequency.

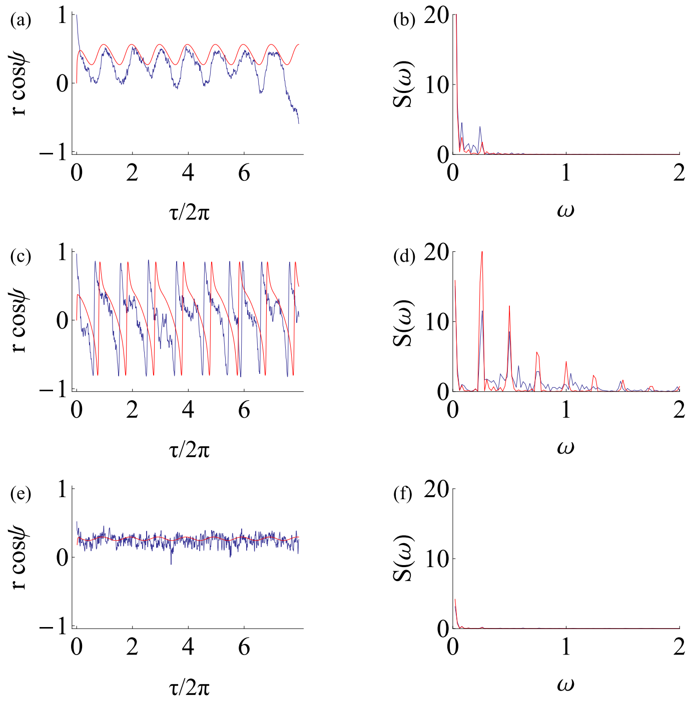

FIG. 10. Stochastic resonance in the numerical simulation of a 400-element coupled DNKA array and comparison to the mean-field DNKA array. Response of a coupled DNKA array to a sinusoidal stimulus of amplitude $f_\Omega = 0.1$ and frequency $\Omega = 0.25$. The parameters of the array are: $D_\theta = 1$, $\Delta = 0.5$, $K = 15$, $f_0 = 1.15$. Left column, parts (a), (c), and (e): the time-dependent real part of the order parameter (vertical axis) vs $\tau/2\pi$. The noise levels are: (a) $D_\theta = 0.5$, (c) $D_\theta = 3$, and (e) $D_\theta = 8$. Red (thin light gray) lines show the DMFT result, and the blue (thick dark gray) lines show the numerically computed order parameter, for an array of 400 oscillators. Right column, parts (b), (d), and (f): corresponding power spectra of the order parameter.

approaches $\Omega = 0$. Note that there is no maximum at Ω/ω_0, so the array exhibits no frequency selectivity. As the stimulus amplitude f_Ω is decreased, the interval of stimulus frequencies over which the array responds to the drive decreases in size. There is a rapid decrease of the output power at low frequencies around $f_\Omega = 0.1$, when the stimulus amplitude drops below the activation threshold of the detector. The linear response regime $f_\Omega < 0.1$ is shown in more detail in Figure 9(b).

Next, we computed the response in the presence of a moderate level of frequency dispersion ($\Delta = 1.5$). The first row of the Figure 9(b) shows that the frequency dispersion degrades the responsiveness, but the enhancement of the signal by SR is still present at low frequencies.

The time trace of the order parameter shows clear SR even with frequency dispersion. Figure 10 shows the time trace of the order parameter with $\Delta = 0.5$. The first row ((a), (b)) shows the effects of introducing a low level of intrinsic noise ($D_\theta = 0.5$). The DMFT order parameter (Figure 10(a), red line(light gray)) shows sinusoidal oscillation. The order parameter of the finite array of 400 oscillators, though noisy, is also roughly sinusoidal (Figure 10(a)), as indicated by the blue (dark gray) line. Interestingly, the oscillation amplitude of the finite array exceeds that of the DMFT. The large “central” peak in the power spectrum (Figure 10(b)) for small ω is the noise-broadened $\omega = 0$ delta function associated with a static order parameter. The response to the applied signal is given by the small peak at 0.25. When the intrinsic noise level is increased to $D_\theta = 2.5$ (Figure 10(c),(d)), the system responds to the stimulus with a regular, high amplitude spike train. The numerically computed order parameter shows similar spikes, though with a lag with respect to the DMFT spike train (Figure 10(c)). The corresponding power spectrum (Figure 10(d)) is a harmonic series, showing integral multiples of the drive frequency. The SNR is very large, about ≈ 10. Finally, for $D_\theta = 8$ (Figure 10(e),(f)), the system again no longer responds to the stimulus. The introduction of a moderate frequency dispersion thus has affected neither the output power nor the SR signal amplification in a significant manner. Unlike the decoupled system, the coupled array *can* function as a sensitive stimulus detector that is robust against the introduction of a significant amount of frequency dispersion.

Could frequency dispersion actually *enhance* the detection sensitivity analogously to the effect of phase noise? The dependence of the output power $S(\Omega)$ at the drive frequency on the dispersion Δ is shown in Figure 11, for different values of the coupling constant K. In the

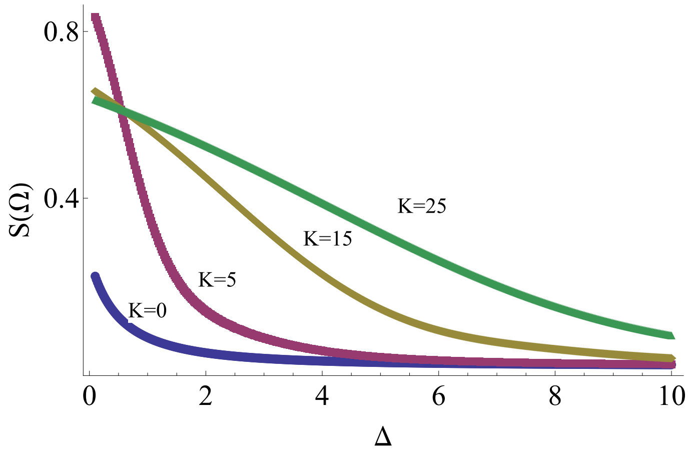

FIG. 11. Power output vs. frequency dispersion, computed using the spectral method. Power at the drive frequency ($\Omega = 0.25$) is plotted as a function of the frequency dispersion Δ, for $f_\Omega = 0.1$, $D_\theta = 0.5$, and $f_0 = 1.15$, for different values of the coupling constant K. The system does not exhibit stochastic resonance with varying frequency dispersion.

DMFT limit, the power output decreases monotonically as a function of Δ for all values of K, showing no indication of stochastic resonance. However, numerical solutions of the equations of motion for 400 oscillators show examples of stochastic resonance effects induced by frequency dispersion. The effect is, however, not consistent: different sets of randomly chosen frequencies, drawn from the same statistical distribution, may or may not show stochastic resonance effects. The effect disappears in the thermodynamic limit.

B. Stimulus detection and the Hopf-Kuramoto transition

The response of the array undergoes a drastic change when it is poised near the line of Hopf-Kuramoto transitions, which occurs at larger values of the static offset and natural frequency (see Figure 5). Parameters were chosen so that the system is in the regime of coherent oscillations for $D_\theta = 0$, with f_0 below ω_0. The line of bifurcations is crossed by increasing the level of phase noise D_θ (see Figure 12).

At the lowest noise level ($D_\theta = 0.02$), the spontaneous oscillations exhibit a large amplitude, and hence, the order parameter is non-zero. Imposing a stimulus introduces two weak side bands into the power spectrum, positioned on opposite sides of the peak at the drive frequency Ω (Figure 12(g)). If the noise level is increased to $D_\theta = 0.9$, then the amplitude of the spontaneous oscillations slowly damps to zero, indicating that the system is poised on the quiescent side of a Hopf-Kuramoto bifurcation (Figure 12(b)). When the stimulus is introduced (Figure 12(e)), the power spectrum shows a robust response at the drive frequency (Figure 12(h)). The response is harmonic, unlike the SNIC case, with only a single peak in the power spectrum. When the noise level is further increased to $D_\theta = 8$ (Figure 12(c), (f), (i)), the amplitude of the response strongly diminishes. The optimal detection sensitivity at intermediate noise levels could be viewed as a remnant of the SR effect.

Figure 12(j) is a plot of the output power at the drive frequency as a function of the coupling constant and D_θ. For increasing D_θ, there is an initial steep rise of the output power. The output power diminishes continuously to zero and vanishes at the Kuramoto synchronization threshold (black line); this transition could be called a Kuramoto-Hopf bifurcation.

Figure 13 shows the output power as a function of the drive frequency and amplitude.It has the shape of a classical Arnold Tongue that extends down to the natural frequency at the lowest drive amplitudes. The array is most sensitive to the stimulus when the stimulus frequency matches the natural frequency ω_0. The detector array now has a reasonable level of *frequency resolution*. It should be recalled however that the individual elements of the array are phase oscillators that do not show an Andronov-Hopf bifurcation: the Andronov-Hopf bifurcation is a collective (or emergent) property of the coupled array.

The observed frequency dependence is similar to a conventional resonance peak. Note that the peak width narrows when the drive amplitude is decreased. This resonance peak of the array of coupled phase-oscillators resembles that of a single Hopf oscillator [7]. However, in this instance, the “quiescent” state of the system is composed of an array of active but mutually incoherent phase oscillators.

V. CONCLUSION

We examined the forced Kuramoto model for an array of coupled phase oscillators in an environment with a substantial level of phase noise and with a substantial level of frequency dispersion between the oscillators. Stimulus detection requires the Kuramoto order-parameter to be finite. We found the impact of phase noise and frequency dispersion on the Kuramoto order parameter to be quite similar. In both cases, there is a threshold where the order-parameter vanishes continuously. In both cases, the onset of quiescence under the application of a steady load is described by an Arnold Tongue, with the quiescent state separated from the oscillatory one by lines of SNIC and Andronov-Hopf bifurcations, joined at

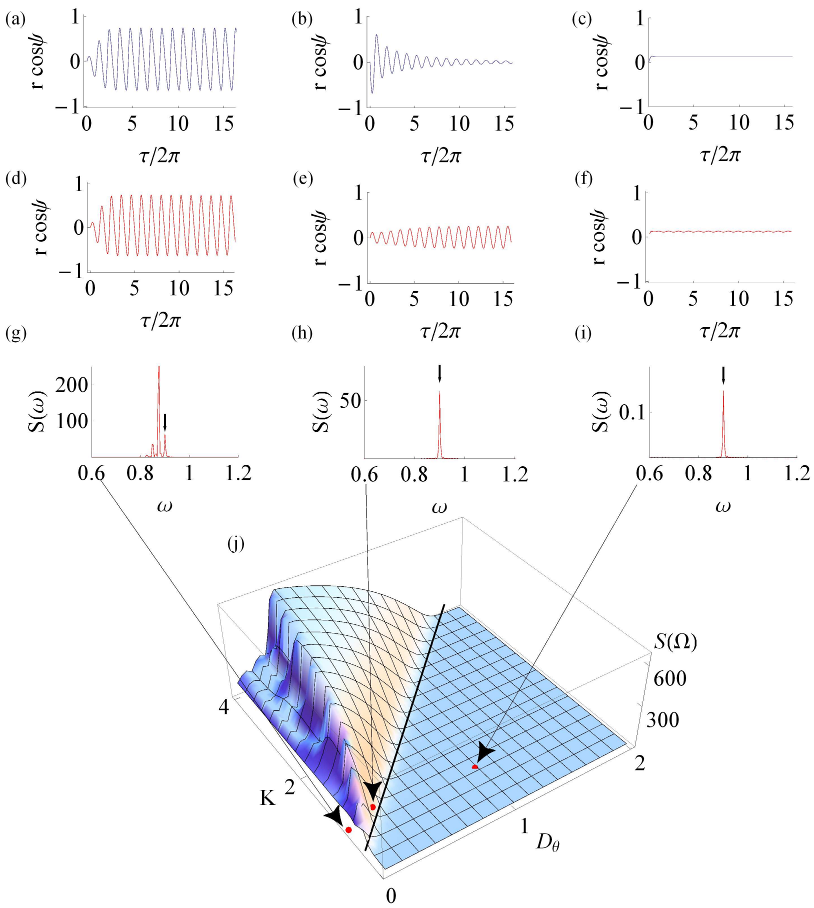

FIG. 12. Response of the coupled DNKA model near a Hopf bifurcation. An array of coupled oscillators, with large frequency dispersion, is subject to a stimulus of frequency $\Omega = 0.9$ and amplitude $f_\Omega = 0.02$. The system parameters are $f_0 = 0.5$, and $\Delta = 0.16$. For panels (a)-(i), the coupling constant is fixed at $K = 0.8$; in panel (j), it is varied. First row: time-dependent real part of the order parameter, without stimulus. Second row: time-dependent real part of the order parameter, with stimulus. Third row: corresponding power spectra, with stimulus. The columns correspond to different phase diffusion coefficients; (a), (d), and (g): $D_\theta = 0.02$; (b), (e), and (h): $D_\theta = 0.2$; (c), (f), and (i): $D_\theta = 1$. Arrows in (g), (h), and (i) indicate the spontaneous frequency of the system. (j) Power output $S(\omega = \Omega)$ as a function of the noise level D_θ and coupling constant K. The black line denotes the Kuramoto-Hopf bifurcation line. The red (gray) dots show the K values used in top panels, as indicated by the arrows.

a Bogdanov-Takens bifurcation point. We further showed that the SNIC bifurcation dominates for larger coupling coefficients while the Andronov-Hopf bifurcation dominates for weaker coupling coefficients.

In contrast, the effects of phase noise and frequency dispersion on stimulus detection are quite different. Near a SNIC bifurcation, with the array functioning as a subtreshold detector, phase noise produces a very pronounced *stochastic resonance* (SR) effect, for an intermediate range of noise intensities. The coupling between the oscillators greatly enhances the sensitivity, but only for an intermediate range of coupling constants, dependent on the noise intensity. Frequency dispersion, on the other hand, only degrades the sensitivity. In summary, the quiescent array poised near a SNIC bifurcation can function as a very sensitive signal detector in the presence of substantial levels of phase noise and frequency dispersion. The amplification is highly nonlinear and shows poor frequency selectivity.

When the array is “tuned” by the applied steady load and noise level D_θ to be poised near the line of Andronov-Hopf bifurcations, a very different form of stimulus detection is encountered. The response of the array has a resonance when the drive frequency equals that of the natural frequency, reminiscent of that of a single Hopf oscillator in the absence of noise. This feature is an emergent property of the array, since the individual oscillators do not exhibit an Andronov-Hopf bifurcation. The stimulus detection of the coupled array near a Hopf-Kuramoto bifurcation transition is robust against the introduction of frequency dispersion and of phase noise.

It was already well known from the work of Kuramoto and others that the decohering effects of both phase noise and frequency dispersion are counteracted by coupling oscillators into an array. It had also been shown earlier [38] that SR is enhanced for a coupled array. The new result of our work is that the ability of the coupled array to function as a sensitive stimulus detector is restricted to

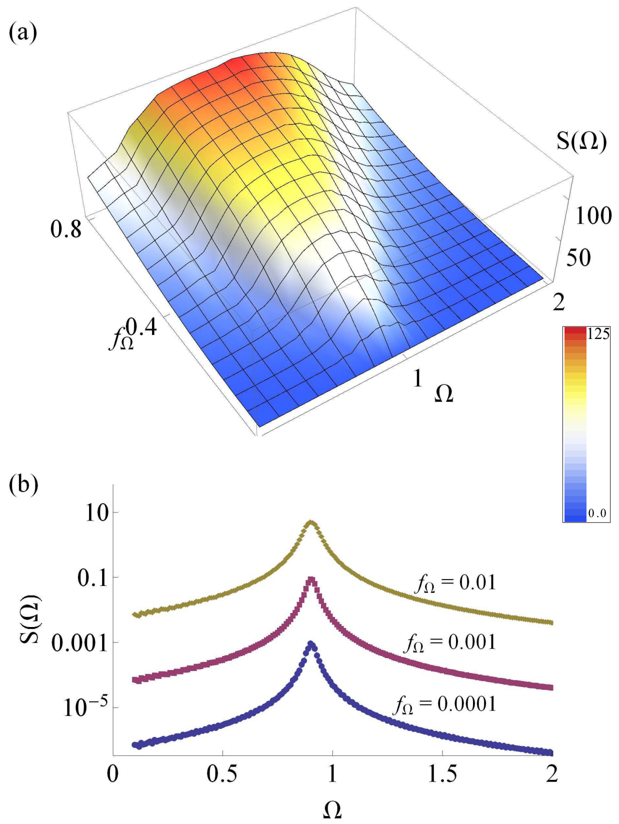

FIG. 13. Frequency selectivity near the Kuramoto-Hopf bifurcation. (a) Power output $S(\omega = \Omega)$ as a function of the stimulus frequency Ω and stimulus amplitude f_Ω, for $D_\theta = 0.2$, $\Delta = 0.16$, $K = 0.8$, and $f_0 = 0.5$. (b) Power output $S(\omega = \Omega)$ as a function of the stimulus frequency Ω, for various values of f_Ω $(0.0001, 0.001, 0.01)$, computed with $K = 0.8$, $D_\theta = 0.2$, $f_0 = 0.5$, and $\Delta = 0.16$.

an *intermediate* range of coupling constants. An overly rigid array does not detect weak stimulus signals.

Another interesting aspect is the relaxation time of the array. Studies of hair cells in the context of the mammalian cochlea normally assume that the oscillators are poised near an Andronov-Hopf bifurcation, where frequency selectivity and sensitivity are maximized. However, the array is intrinsically very slow near the Hopf critical point, which could lead to a form of *critical slowing down*. Figure 12(b) shows that critical slowing down is also a feature of the present system for the case that the array is poised near the line of Hopf-Kuramoto transitions. However, when the coupled oscillators are poised near the SNIC line, then the response is fast, as shown in Figure 8. The array is a very sensitive and very fast detector of low frequency signals, which would seem consistent with the biological function of the AS. Future quantitative tests could focus on the question whether signal detection by the AS is based on SR, which could be tested by adding synthetic noise and measuring the dependence of the SNR on the noise intensity.

An interesting outcome of our study is that the same array can operate either as a SNIC or as a Hopf based stimulus detector. Low-frequency detection of seismic signals could be based on a coupled array of phase oscillators poised near a SNIC bifurcation. A comparable model, with different frequency dispersion and coupling characteristics, could be poised near the Andronov-Hopf bifurcation, and hence exhibit frequency selectivity. Different versions of the current model could therefore reproduce a rich array of phenomenology exhibited by different vestibular and auditory end organs of different species.

VI. ACKNOWLEDGMENTS

The authors would like to thank Dr. Roie Shlomovitz for his assistance with the numerical simulation code. RB would like to thank the NSF for support under DMR Grant No. 1006128. DB would like to thank NSF for support under grant IOS 1257817.

[1] A. J. Hudspeth, Neuron **59**, 530 (2008).
[2] W. Bialek, Ann. Rev. Biophys. Biophys. Chem. **16**, 455 (1987).
[3] M. A. Vollrath, K. Y. Kwan, and D. P. Corey, Annu Rev Neurosci **30**, 339 (2007).
[4] A. J. Hudspeth, in *Principles of Neural Science*, edited by S.-J. H. Kandel, E. R. and T. M. Jessell (McGraw-Hill, New York, 2000) pp. 590–624.
[5] H. L. F. Helmholtz, *On the sensations of tone as a physiological basis for the theory of music* (Dover Publications, New York, 1954).
[6] T. Gold, Proceedings of the Royal Society of London B **135**, 492 (1948).
[7] V. M. Eguiluz, M. Ospeck, Y. Choe, A. J. Hudspeth, and M. O. Magnasco, Phys Rev Lett **84**, 5232 (2000).
[8] S. Camalet, T. Duke, F. Jülicher, and J. Prost, Proc Natl Acad Sci U S A **97**, 3183 (2000).
[9] Y. Choe, M. O. Magnasco, and A. J. Hudspeth, Proc Natl Acad Sci U S A **95**, 15321 (1998).
[10] T. Duke and F. Jülicher, Phys Rev Lett **90**, 158101 (2003).
[11] S. H. Strogatz, *Nonlinear Dynamics and Chaos* (Westview Press, Cambridge, MA, 1994).
[12] P. Martin and A. J. Hudspeth, Proc Natl Acad Sci U S A **98**, 14386 (2001).
[13] J. Barral and P. Martin, PNAS **109**, E1344 (2012).
[14] R. B. Lea Fredrickson-Hemsing, Seung Ji and D. Bozovic, Phys Rev E **86**, 021915 (2012).
[15] M. S. Smotherman and P. M. Narins, J Exp Biol **203**, 2237 (2000).
[16] P. Martin, A. J. Hudspeth, and F. Jülicher, Proc Natl Acad Sci U S A **98**, 14380 (2001).
[17] Y. Roongthumskul, R. Shlomovitz, R. Bruinsma, and D. Bozovic, Phys Rev Lett **110**, 148103 (2013).

[18] L. Glass and M. C. Mackey, *From Clocks to Chaos* (Princeton University Press, 1988).
[19] P. M. Kachar, B. and J. Fex, Hearing Research **45**, 179 (1990).
[20] C. E. Strimbu, D. Ramunno-Johnson, L. Fredrickson, K. Arisake, and D. Bozovic, Hearing Research **256**, 58 (2009).
[21] C. E. Strimbu, L. Fredrickson-Hemsing, and D. Bozovic, PLoS ONE **7** (2012).
[22] R. Shlomovitz, Y. Roongthumskul, S. Ji, D. Bozovic, and R. Bruinsma, Interface focus **4**, 20140022 (2014).
[23] D. Ramunno-Johnson, C. Strimbu, L. Fredrickson, K. Arisaka, and D. Bozovic, Biophysical Journal **96**, 1159 (2009).
[24] B. L. F. J. Jeremie Barral, Kai Dierkes and P. Martin, PNAS **107**, 8079 (2010).
[25] K. Dierkes, B. Lindner, and F. Jülicher, Proc Natl Acad Sci U S A **105**, 18669 (2008).
[26] T. Risler, J. Prost, and F. Jülicher, Physical review letters **93**, 175702 (2004).
[27] K.-H. Ahn, Journal of The Royal Society Interface **10** (2013), 10.1098/rsif.2013.0525.
[28] L. M. Childs and S. H. Strogatz, CHAOS **18**, (2008).
[29] L. Gammaitoni, P. Hänggi, P. Jung, and F. Marchesoni, Rev. Mod. Phys. **70**, 223 (1998).
[30] B. Nadrowski, P. Martin, and F. Jülicher, Proc Natl Acad Sci U S A **101**, 12195 (2004).
[31] A. K. Yuttana Roongthumskul, Lea Fredrickson-Hemsing and D. Bozovic, Biophysical Journal **101**, 603 (2011).
[32] See Supplementary Material.
[33] H. Sakaguchi, S. Shinomoto, and Y. Kuramoto, Progress of Theoretical Physics **79**, 600 (1988).
[34] J. A. Acebron, L. L. Bonilla, C. J. Perez Vicente, F. Ritort, and R. Spigleri, REVIEWS OF MODERN PHYSICS **77**, (2005).
[35] A. Arenas and C. J. P. Vicente, Physical review E **50**, 949 (1994).
[36] A.-V. N. A. V. T. Anishchenko, V. S. and L. Schimansky-Geier, *Nonlinear Dynamics of Chaotic and Stochastic Systems* (Springer, Berlin Heidelberg, 2007).
[37] M. A. Zaks, A. B. Neiman, S. Feistel, and L. Schimansky-Geier, Physical Review E **68**, 066206 (2003).
[38] M. E. Inchiosa and A. R. Bulsara, Physical Review E **52**, 327 (1995).
[39] K. Watanabe, ZAMM-Journal of Applied Mathematics and Mechanics/Zeitschrift für Angewandte Mathematik und Mechanik **90**, 151 (2010).

APPENDIX

A. Coupling constant estimation from 2D Green's function

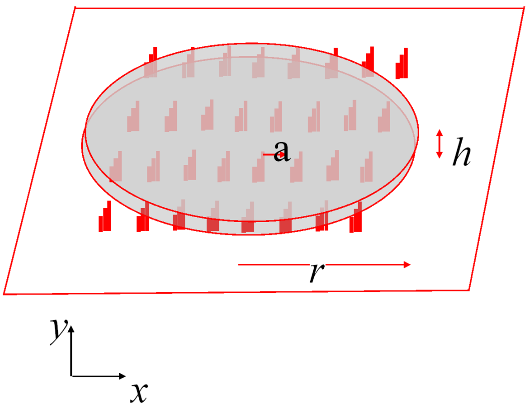

FIG. 14. Schematic diagram of 2D membrane

We can model the AS as a system of nonlinear oscillators coupled by a 2D elastic sheet. 2D Green's function for the homogeneous medium is given by [39]

$$G_{x,x}(r,\theta) = \frac{\gamma^2-1}{4\pi\gamma^2\mu}\left\{-\frac{\gamma^2+1}{\gamma^2-1}\log(r) + \cos^2\theta\right\} \quad (14)$$

$$G_{x,y}(r,\theta) = \frac{\gamma^2-1}{4\pi\gamma^2\mu}\frac{\sin(2\theta)}{2} \quad (15)$$

$$G_{y,y}(r,\theta) = \frac{\gamma^2-1}{4\pi\gamma^2\mu}\left\{-\frac{\gamma^2+1}{\gamma^2-1}\log(r) - \cos^2\theta\right\} \quad (16)$$

where $\gamma^2 = \frac{\lambda+2\mu}{\mu}$, and λ and μ are Lame's constants. The displacement at i^{th} site due to all the forces is,

$$u_{i,x} = \sum_k [G_{x,x}(r_{i,k},\theta_{i,k})f_{k,x} + G_{x,y}(r_k,\theta_k)f_{k,y}] \quad (17)$$

$$u_{i,y} = \sum_k [G_{y,y}(r_{i,k},\theta_{i,k})f_{k,y} + G_{y,x}(r_k,\theta_k)f_{k,x}] \quad (18)$$

We assume that the forces are exerted only in the x direction,

$$u_{i,x} = \sum_k G_{x,x}(r_{i,k},\theta_{i,k})f_{k,x} \quad (19)$$

$$u_{i,y} = \sum_k G_{y,x}(r_{i,k},\theta_{i,k})f_{k,x} \quad (20)$$

Moreover, we are interested in the bundle motion in x-direction only. As a result, the equation looks similar to predictions based on the scalar elasticity theory:

$$u_{i,x} = \sum_k G_{x,x}(r_{i,k},\theta_{i,k})f_{k,x} \quad (21)$$

$$= \int_0^{2\pi} \mathrm{d}\theta G_{x,x}(r_{i,i},\theta_{i,i})f_{i,x} + \sum_{k,k\neq i} < G_{x,x}(r_{i,k},\theta_{i,k}) > f_{k,x} \quad (22)$$

Then, the difference between the scalar Green's Function and the 2D Green's function is given by the angle dependence of the latter. Here, we can define hair bundle density function such that

$$\rho = \begin{cases} N/(\pi \mathsf{r}^2) \text{ if } a < r < \mathsf{r} \\ 0 \text{ if } \mathsf{r} < r < R \end{cases} \quad (23)$$

Then the average Green's function is,

$$\frac{1}{N}\int \mathrm{d}^2 r G_{x,x}(r,0)\rho \quad (24)$$

$$= \int_0^{2\pi}\int_a^{\mathsf{r}} r\,\mathrm{d}r\,\mathrm{d}\theta \frac{\gamma^2-1}{4\pi\gamma^2\mu}\left\{-\frac{\gamma^2+1}{\gamma^2-1}\log(r) + \cos^2\theta\right\}\frac{1}{\pi\mathsf{r}^2}$$

$$= \frac{-1}{4\pi\mathsf{r}^2\mu}[\mathsf{r}^2\log\mathsf{r} - a^2\log a - \mathsf{r}^2 + a^2]$$

$$+ \frac{-1}{4\pi\gamma^2\mathsf{r}^2\mu}[\mathsf{r}^2\log\mathsf{r} - a^2\log a]$$

$$< G > \approx \frac{-1}{4\pi\mu}[\log\mathsf{r} - 1] + \frac{-1}{4\pi\gamma^2\mu}[\log\mathsf{r}] \quad (25)$$

$$G_0 = \frac{1}{2\pi}\int_0^{2\pi}\mathrm{d}\theta G_{x,x}(r_{i,i},\theta_{i,i})$$

$$= \frac{\gamma^2-1}{4\pi\gamma^2\mu}\left\{-\frac{\gamma^2+1}{\gamma^2-1}\log(a) + \frac{1}{2}\right\} \quad (26)$$

Then, we can find the force in terms of displacements by inverting the matrix.

$$
\begin{aligned}
f_i &= \frac{1}{N}\left[\frac{1}{< G_{x,x}(r_{i,j},\theta_{i,j}) > -G_0}\sum_j (u_{j,x}-u_{i,x})\right] \\
&= \frac{1}{N}\left[\frac{1}{\frac{-1}{4\pi\mu}[\frac{1}{2}\log \mathsf{r}-1]+\frac{-1}{4\pi\gamma^2\mu}[\frac{1}{2}\log \mathsf{r}]-\frac{\gamma^2-1}{4\pi\gamma^2\mu}\left\{-\frac{\gamma^2+1}{\gamma^2-1}\log(a)+\frac{1}{2}\right\}}\sum_j (u_{j,x}-u_{i,x})\right] \\
&\approx \frac{1}{N}\frac{-4\pi\gamma\mu}{(\frac{1}{2}-\log\frac{\mathsf{r}}{a})(\gamma+\frac{1}{\gamma})}\sum_j (u_{j,x}-u_{i,x}) \\
&\approx \frac{1}{N}\frac{-4\pi\mu(\kappa+\mu)}{\kappa+2\mu}\frac{1}{(\frac{1}{2}-\log\frac{\mathsf{r}}{a})}\sum_j (u_{j,x}-u_{i,x})
\end{aligned} \tag{27}
$$

where κ is bulk modulus, and μ is shear modulus for 2-D($\kappa = \lambda + \mu$). Define C to be:

$$
C = \frac{-4\pi\mu(\kappa+\mu)}{\kappa+2\mu}\frac{1}{(\frac{1}{2}-\log\frac{\mathsf{r}}{a})} \tag{28}
$$

The final answer obtained is hence similar to the scalar case.

1. *Conversion to the Adler equation*

Fourier Transform of the equation (27) yields:

$$
f_i(\omega) = \frac{1}{N}C\sum_j (u_{j,x}(\omega)-u_{i,x}(\omega)) \tag{29}
$$

We then substitute the force into the linear response equation:

$$
u_{i,x}(\omega) = \chi(\omega)f_i(\omega) \tag{30}
$$

$$
\begin{aligned}
u_{i,x}(\omega) &= \chi(\omega)\frac{1}{N}C\sum_j (u_{j,x}(\omega)-u_{i,x}(\omega)) \\
&= \frac{\Gamma}{i(\omega-\omega_i)-\nu}\frac{C}{N}\sum_j (u_{j,x}(\omega)-u_{i,x}(\omega))
\end{aligned} \tag{31}
$$

$$
\begin{aligned}
&u_{i,x}(\omega)(1-\frac{C\Gamma}{i(\omega-\omega_i)-\mu}) \\
&= \frac{\Gamma}{i(\omega-\omega_i)-\nu}\frac{-C}{N}\sum_j (u_{j,x}(\omega))
\end{aligned} \tag{32}
$$

$$
\begin{aligned}
&u_{i,x}(\omega)((i(\omega-\omega_i)-\nu)+C\Gamma) \\
&= \frac{C\Gamma}{N}\sum_j (u_{j,x}(\omega))
\end{aligned} \tag{33}
$$

$$
\begin{aligned}
&u_{i,x}(\omega)(i(\omega-\omega_i)-(\nu-C\Gamma)) \\
&= \frac{C\Gamma}{N}\sum_j (u_{j,x}(\omega))
\end{aligned} \tag{34}
$$

We obtain the equation for $u_{i,x}$ by inverse Fourier transform:

$$
\dot{u}_{i,x}(t) = (i(\omega_i)+(\nu-C\Gamma))u_{i,x}(t)+\frac{C\Gamma}{N}\sum_j (u_{j,x}(t)) \tag{35}
$$

Let $u_{i,x} = Ae^{i\theta_i}$. Then,

$$
\dot{\theta} = ((\omega_i)-i(\nu-C\Gamma))-i\frac{C\Gamma}{N}\sum_j (e^{i(\theta_j-\theta_i)}) \tag{36}
$$

$$
\dot{\theta} = \omega_i + \frac{C\Gamma}{N}\sum_j \sin(\theta_j-\theta_i) \tag{37}
$$

$$
0 = -(\nu-C\Gamma)+\frac{C\Gamma}{N}\sum_j \cos(\theta_j-\theta_i) \tag{38}
$$

Thus, the coupling constant for the Kuramoto model is

$$
K = \frac{-4\pi\mu(\kappa+\mu)\Gamma}{\kappa+2\mu}\frac{1}{(\frac{1}{2}-\log\frac{\mathsf{r}}{a})}
$$

.

B. stationary state solution

The stationary solution of eq.10 can be written as follows:

$$
\rho_{st} = e^{(\omega_0\theta+Kr\cos(\psi-\theta)+f_0\cos\theta)/D_\theta}\left[N-\frac{S}{D_\theta}\int_0^\theta e^{-(\omega_0 x+Kr\cos(\psi-x)+f_0\cos x)/D_\theta}\,\mathrm{d}x\right] \tag{39}
$$

where S is the probability current, and N is the normalization constant. S and N can be found from the normalization condition and the periodicity of ρ.

$$
\int_0^{2\pi}\rho_{st}\,\mathrm{d}\theta = 1
$$

$$
\rho_{st}(\theta) = \rho_{st}(\theta+2\pi)
$$

The result is:

$$N = \left[I_- - \frac{1}{I_+} \int_0^{2\pi} \int_0^{\theta} e^{-(V(\theta)-V(x))/D_\theta} \, \mathrm{d}x \, \mathrm{d}\theta \right]^{-1} \tag{40}$$

$$S = \frac{D_\theta}{I_+}(1 - e^{-2\pi\omega_0/D_\theta}) \tag{41}$$

$$\left[I_- - \frac{1}{I_+}(1 - e^{-2\pi\omega_0/D_\theta}) \int_0^{2\pi} \int_0^{\theta} e^{-(V(\theta)-V(x))/D_\theta} \, \mathrm{d}x \, \mathrm{d}\theta \right]^{-1}$$

where $V(\theta) = -\omega_0\theta - Kr\cos(\psi - \theta) - f_0\cos\theta$ and $I_\pm = \int_0^{2\pi} e^{\pm V(x)/D_\theta} \, \mathrm{d}x$. Substituting N and S into the ρ_{st} and simplifying the equation, we obtain the final form:

$$\rho_{st}(\theta, \omega_0) = \frac{A(\theta) \int_0^{2\pi} B(\theta, x) \, \mathrm{d}x}{Z} \tag{42}$$

where $A(\theta) = e^{(Kr\cos(\psi-\theta)+f_0\cos\theta)/D_\theta}$, $B(\theta, x) = e^{-(\omega_0 x + Kr\cos(\psi-\theta-x)+f_0\cos(\theta+x))/D_\theta}$, and $Z = \int_0^{2\pi} A(\theta) \int_0^{2\pi} B(\theta, x) \, \mathrm{d}x \, \mathrm{d}\theta$. Here, we can redefine generating function Z,

$$Z = \int_0^{2\pi} e^{(\sigma\cos(\psi-\phi)-\eta\cos\theta)} \int_0^{2\pi} e^{-(\omega_0 x + Kr\cos(\psi-\theta-x)+f_0\cos(\theta+x))/D_\theta} \, \mathrm{d}x \, \mathrm{d}\theta \tag{43}$$

which can be written in terms of a series of Modified Bessel functions of the first kind:

$$Z = (1 - e^{2\pi\omega_0/D_\theta}) \left[\frac{-\pi}{2} \sum\sum\sum (-1)^{m+p} I_m(Kr/D_\theta) I_p(\eta) I_l(\sigma) H(\psi, \phi, -f_0/D_\theta, \omega_0) \right] \tag{44}$$

$$\begin{aligned} H = {} & I_{l+p-m}(-f_0/D_\theta) \frac{\frac{-\omega_0}{D_\theta}\cos(l\phi - m\psi) + (l+p)\sin(l\phi - m\psi)}{(\frac{\omega_0}{D_\theta})^2 + (l+p)^2} \\ & + I_{l-p-m}(-f_0/D_\theta) \frac{\frac{-\omega_0}{D_\theta}\cos(l\phi - m\psi) + (l-p)\sin(l\phi - m\psi)}{(\frac{\omega_0}{D_\theta})^2 + (l-p)^2} \\ & + I_{l+p+m}(-f_0/D_\theta) \frac{\frac{-\omega_0}{D_\theta}\cos(l\phi + m\psi) + (l+p)\sin(l\phi + m\psi)}{(\frac{\omega_0}{D_\theta})^2 + (l+p)^2} \\ & + I_{l-p+m}(-f_0/D_\theta) \frac{\frac{-\omega_0}{D_\theta}\cos(l\phi + m\psi) + (l-p)\sin(l\phi + m\psi)}{(\frac{\omega_0}{D_\theta})^2 + (l-p)^2} \end{aligned} \tag{45}$$

Then, the order parameter r and higher order terms can be written in terms of the generating functional:

$$\begin{aligned} r &= \left\langle \frac{\partial \log Z}{\partial \sigma} |_{\sigma=Kr/D_\theta, \eta=-f_0/D_\theta, \phi=\psi} \right\rangle \\ &= \int\int \frac{\sum\sum\sum(-1)^{m+p} I_m(Kr/D_\theta) I_p(-f_0/D_\theta) I_{l+1}(Kr/D_\theta) H(\psi, -f_0/D_\theta, \omega_0)}{\sum\sum\sum(-1)^{m+p} I_m(Kr/D_\theta) I_p(-f_0/D_\theta) I_l(Kr/D_\theta) H(\psi, -f_0/D_\theta, \omega_0)} g(\omega_0) F(f_0) \, \mathrm{d}\omega_0 \, \mathrm{d}f_0 \end{aligned} \tag{46}$$

$$\begin{aligned} \sigma^2 &= \left\langle \frac{1}{Z} \frac{\partial^2 Z}{\partial \sigma^2} |_{\sigma=Kr/D_\theta, \eta=-f_0/D_\theta, \phi=\psi} \right\rangle \\ &= \frac{1}{2} + \int\int \frac{1}{2} \frac{\sum\sum\sum(-1)^{m+p} I_m(Kr/D_\theta) I_p(-f_0/D_\theta) I_{l+2}(Kr/D_\theta) H(\psi, -f_0/D_\theta, \omega_0)}{\sum\sum\sum(-1)^{m+p} I_m(Kr/D_\theta) I_p(-f_0/D_\theta) I_l(Kr/D_\theta) H(\psi, -f_0/D_\theta, \omega_0)} g(\omega_0) F(f_0) \, \mathrm{d}\omega \, \mathrm{d}f_0 \end{aligned} \tag{47}$$

$$\begin{aligned}
< \sin\eta > &= \frac{1}{\sigma Z}\frac{\partial Z}{\partial \phi}|_{\sigma=Kr/D_\theta,\eta=h/D_\theta,\phi=\psi} \qquad (48)\\
&= \frac{D_\theta}{Kr}\int\int \frac{\sum\sum\sum(-1)^{m+p}I_m(Kr/D_\theta)I_p(-f_0/D_\theta)I_l(Kr/D_\theta)\frac{\partial H(\psi,-f_0/D_\theta,\omega_0)}{\partial\phi}}{\sum\sum\sum(-1)^{m+p}I_m(Kr/D_\theta)I_p(-f_0/D_\theta)I_l(Kr/D_\theta)H(\psi,-f_0/D_\theta,\omega_0)} g(\omega_0)F(f_0)\,\mathrm{d}\omega_0\,\mathrm{d}f_0\\
< \sin\eta\cos\eta > &= \frac{1}{\sigma}(\frac{1}{Z}\frac{\partial^2 Z}{\partial\phi\partial\sigma} - \frac{1}{\sigma Z}\frac{\partial Z}{\partial\phi})|_{\sigma=Kr/D_\theta,\eta=h/D_\theta,\phi=\psi} \qquad (49)\\
&= \frac{D_\theta}{Kr}(\int\int \frac{\sum\sum\sum(-1)^{m+p}I_m(Kr/D_\theta)I_p(-f_0/D_\theta)I_{l+1}(Kr/D_\theta)\frac{\partial H(\psi,-f_0/D_\theta,\omega_0)}{\partial\phi}}{\sum\sum\sum(-1)^{m+p}I_m(Kr/D_\theta)I_p(-f_0/D_\theta)I_l(Kr/D_\theta)H(\psi,-f_0/D_\theta,\omega_0)} g(\omega_0)F(f_0)\,\mathrm{d}\omega_0\,\mathrm{d}f_0\\
&- \frac{D_\theta}{Kr}\int\int \frac{\sum\sum\sum(-1)^{m+p}I_m(Kr/D_\theta)I_p(-f_0/D_\theta)I_l(Kr/D_\theta)\frac{\partial H(\psi,-f_0/D_\theta,\omega_0)}{\partial\phi}}{\sum\sum\sum(-1)^{m+p}I_m(Kr/D_\theta)I_p(-f_0/D_\theta)I_l(Kr/D_\theta)H(\psi,-f_0/D_\theta,\omega_0)} g(\omega_0)F(f_0)\,\mathrm{d}\omega_0\,\mathrm{d}f_0)
\end{aligned}$$

For further calculations, we assume $g(\omega_0)$ to be Lorentzian. Since G is the only frequency dependent term, the frequency integration is performed only on G, yielding

$$\begin{aligned}
\int g(\omega_0)G\,\mathrm{d}\omega &= I_{l+p-m}(-f_0/D_\theta)\left\{\left[(\frac{\omega_0}{D_\theta})^2 + (\frac{\Delta}{D_\theta})^2 + (l+p)^2\right]^2 - 4(l+p)^2(\frac{\Delta}{D_\theta})^2\right\}^{-1} \qquad (50)\\
&\{\frac{-\omega_0}{D_\theta}\cos(l\phi - m\psi)\left[(\frac{\omega_0}{D_\theta})^2 + (\frac{\Delta}{D_\theta})^2 + (l+p)^2 - 2\frac{\Delta}{D_\theta}(l+p)\right]\\
&+ (l+p)\sin(l\phi - m\psi)\left[(\frac{\omega_0}{D_\theta})^2 - (\frac{\Delta}{D_\theta})^2 + (l+p)^2\right]\\
&+ \frac{\Delta}{D_\theta}\sin(l\phi - m\psi)\left[(\frac{\omega_0}{D_\theta})^2 + (\frac{\Delta}{D_\theta})^2 - (l+p)^2\right]\}\\
&....
\end{aligned}$$

When the solution is solved numerically, the series needs to be truncated. In this paper, terms with $l > 10$, $p > 10$, and $m > 10$ are set to zero, when the linear stability analysis is performed using MatCont.